

The flickering radio jet from the quiescent black hole X-ray binary A0620-00

Donna L. dePolo,^{1*} Richard M. Plotkin,¹ James C. A. Miller-Jones,² Jay Strader,³ Thomas J. Maccarone,⁴ Tyrone N. O’Doherty,² Laura Chomiuk,³ Elena Gallo⁵

¹Physics Department, University of Nevada, Reno, 1664 N. Virginia St., Reno, NV 89557, USA

²International Centre for Radio Astronomy Research-Curtin University, Perth, WA 6845, Australia

³Center for Data Intensive and Time Domain Astronomy, Department of Physics and Astronomy, Michigan State University, East Lansing, MI 48824, USA

⁴Department of Physics and Astronomy, Texas Tech University, Lubbock TX 79409-1051, USA

⁵Department of Astronomy, University of Michigan, 1085 S University, Ann Arbor, MI 48109, USA

Accepted XXX. Received YYY; in original form ZZZ

ABSTRACT

Weakly accreting black hole X-ray binaries launch compact radio jets that persist even in the quiescent spectral state, at X-ray luminosities $\lesssim 10^{-5}$ of the Eddington luminosity. However, radio continuum emission has been detected from only a few of these quiescent systems, and little is known about their radio variability. Jet variability can lead to misclassification of accreting compact objects in quiescence, and affects the detectability of black hole X-ray binaries in next-generation radio surveys. Here we present the results of a radio monitoring campaign of A0620–00, one of the best-studied and least-luminous known quiescent black hole X-ray binaries. We observed A0620–00 at 9.8 GHz using the Karl G. Jansky Very Large Array on 31 epochs from 2017 to 2020, detecting the source $\sim 75\%$ of the time. We see significant variability over all timescales sampled, and the observed flux densities follow a lognormal distribution with $\mu = 12.5 \mu\text{Jy}$ and $\sigma = 0.22$ dex. In no epoch was A0620–00 as bright as in 2005 ($51 \pm 7 \mu\text{Jy}$), implying either that this original detection was obtained during an unusually bright flare, or that the system is fading in the radio over time. We present tentative evidence that the quiescent radio emission from A0620–00 is less variable than that of V404 Cyg, the only other black hole binary with comparable data. Given that V404 Cyg has a jet radio luminosity ~ 20 times higher than A0620–00, this comparison could suggest that less luminous jets are less variable in quiescence.

Key words: black hole physics – stars: individual: A0620–00 – X-rays: binaries – accretion

1 INTRODUCTION

Transient black hole X-ray binaries (BHXBs) spend the majority of their time experiencing very low levels of accretion in a state of quiescence, which we define by X-ray luminosities $L_X \lesssim 10^{-5} L_{\text{Edd}}$ ¹ (Plotkin et al. 2013). There is growing evidence that quiescent BHXBs launch relativistic outflows in the form of partially self-absorbed synchrotron jets (Blandford & Königl 1979), analogous to the compact radio jets ubiquitously observed from outbursting BHXBs in the hard X-ray spectral state (Fender 2001; Corbel & Fender 2002). However, due to their low radio luminosities, we currently have radio detections of jets from only seven quiescent systems: A0620–00 (Gallo et al. 2006; Dinçer et al. 2018), BW Cir (Plotkin et al. 2021), GX 339–4 (Tremou et al. 2020), MAXI J1348–630 (Carotenuto et al. 2022), MWC 656 (Dzib et al. 2015; Ribó et al. 2017), V404 Cygni (Hjellming et al. 2000; Gallo et al. 2005; Hynes et al. 2009; Rana et al. 2016), and XTE J1118+480 (Gallo et al. 2014), which launch jets with radio luminosities ranging from $\approx 10^{26} - 10^{28}$ erg s^{−1}. Lack of radio detections from other quiescent systems does not prove the absence of jets, however, since it is plausible that current

radio observations are simply not sensitive enough (e.g., Miller-Jones et al. 2011; Plotkin et al. 2016; Rodriguez et al. 2020). One factor, among several, that makes detecting quiescent radio jets challenging is that their level of flux variability is poorly constrained. In turn, interpreting radio observations typically requires coordinating radio campaigns with (strictly simultaneous) observations at other wavebands, especially in the X-ray (see, e.g., Rodriguez et al. 2020, and references therein).

The vast majority of current BHXBs were identified via enhanced X-ray emission during an outburst, which leads to biases in the current BHXB population to objects with, e.g., longer orbital periods, lower inclinations, lower black hole masses, and/or lower line-of-sight absorption (e.g., Narayan & McClintock 2005; Jonker et al. 2021). Identifying BHXBs in quiescence can alleviate some biases, and various strategies have been suggested (and executed) to find quiescent BHXBs via electromagnetic signatures of accretion (e.g., Maccarone 2005; Jonker et al. 2014; Casares 2018), via dynamical searches of detached systems (Giesers et al. 2019; Thompson et al. 2019), and (for binary black holes) through gravitational wave events (Abbott et al. 2016). Radio surveys to discover quiescent BHXBs via their relativistic jets have been suggested and performed (e.g., Maccarone 2005; Shishkovsky et al. 2020; Tudor et al. 2022), and such surveys are revealing intriguing radio-selected candidates (e.g., Tetarenko

* E-mail: donna.depolo@nevada.unr.edu

¹ $L_{\text{Edd}} = 1.3 \times 10^{38} (M_{\text{BH}}/M_{\odot})$ is the Eddington luminosity.

et al. 2016), particularly within globular clusters (e.g., Strader et al. 2012; Chomiuk et al. 2013; Miller-Jones et al. 2015; Shishkovsky et al. 2018; Urquhart et al. 2020; Zhao et al. 2020). However, it is practically impossible to coordinate the requisite strictly simultaneous multiwavelength observations with the initial radio survey observations. Preliminary identifications of radio-selected BHXB candidates can become more reliable by improving characterisation of the level of variability displayed by quiescent radio jets.

Plotkin et al. (2019) performed the first large radio variability study of a quiescent BHXB, focusing on V404 Cygni, which is one of the brightest BHXBs in quiescence (X-ray luminosity $L_X \approx 10^{33}$ erg s⁻¹, or equivalently $\approx 10^{-6}L_{\text{Edd}}$; Bernardini & Cackett 2014). From analyzing 24 years worth of observations in the Karl G. Jansky Very Large Array (VLA) archive, they found that flux densities of V404 Cygni follow a lognormal distribution with a mean $\langle \log(f_\nu/\text{mJy}) \rangle = -0.53$ and a standard deviation of ± 0.30 dex at 8.4 GHz (based on 89 observations), corresponding to an average radio luminosity $L_R \approx 10^{28}$ erg s⁻¹. They also concluded that factor of 2–4 variations are common on timescales ranging from minutes to decades, and those variations are consistent with either flicker noise or white noise. Combining these results with previously identified flaring behaviour on timescales of tens of minutes to hours (e.g., Miller-Jones et al. 2008) suggests that the radio variability of V404 Cygni is consistent with a damped random walk, which may be caused by shocks propagating through a steady, compact jet (Plotkin et al. 2019).

In an effort to continue the characterisation of quiescent radio jet variations, we repeat a similar analysis on the BHXB A0620–00 in quiescence. A0620–00 is a natural choice for the next target in this type of analysis because it is ≈ 100 –200 times less luminous in the X-ray compared to V404 Cygni, such that A0620–00 and V404 Cygni effectively bookend the BHXB quiescent state (for currently known BHXBs). Yet, at a distance of 1.06 ± 0.12 kpc (Cantrell et al. 2010), compared to V404 Cygni’s distance of 2.39 ± 0.14 kpc (Miller-Jones et al. 2009), A0620–00 still has a high enough flux density for a radio monitoring campaign. A0620–00 was discovered during an outburst in 1975 (Elvis et al. 1975), and upon its return to quiescence was dynamically confirmed to contain a black hole ($6.61 \pm 0.25M_\odot$) and a K-type star of mass $0.40 \pm 0.04M_\odot$ (McClintock & Remillard 1986; Cantrell et al. 2010), with an orbital period of 7.75234 ± 0.00010 hours (McClintock & Remillard 1986; González Hernández et al. 2014). Besides the 1975 outburst, only one other historical outburst is known from photographic plates in 1917 (Eachus et al. 1976). A radio outflow was first discovered from A0620–00 in quiescence by Gallo et al. (2006), who reported a radio flux density of $51.1 \pm 6.9 \mu\text{Jy}$ at a central frequency of 8.5 GHz. The only other published radio detection of A0620–00 was by Dinçer et al. (2018), who reported a radio flux density of $26 \pm 8 \mu\text{Jy}$ (8.5 GHz). The above indicates a factor of ≈ 2 variability. However, this is based on only two observations taken eight years apart (observations in 2005 and 2013) with no radio detections between to bridge the observational gap.² It is thus unclear if the factor of ≈ 2 decrease in flux density represents a long-term dimming of the radio jet, or if the 2005 versus 2013 observations happened to catch A0620–00 while it exhibited different levels of (stochastic) variability. Subsequently, in 2016, the jet of A0620–00 was detected by Gallo et al. (2019) at millimetre wavelengths with the Atacama Large Millimeter/submillimeter Array (ALMA); they

² To our knowledge, the only other published observation at GHz frequencies was in 2010 with the Australia Telescope Compact Array, which yielded a non-detection to a $5\sigma_{\text{rms}}$ limit of $<80 \mu\text{Jy}$ (Froning et al. 2011).

Table 1. Summary of each radio observation included in this investigation. Column (1): the calendar date. Column (2): the Modified Julian Date. Column (3): the project code for the VLA. Column (4): the array configuration at the time of observation. Column (5): the total observing time on A0620–00 in minutes. Column (6): the flux density at 9.8 GHz in units of μJy . For non-detections, upper limits are presented at the $2\sigma_{\text{rms}}$ level.

Date	MJD	Project ID	Config	t_{src} (min)	$f_{9.8}$ (μJy)
2017 Sept. 11	58007.5977	17B-233	B	20	28.2 \pm 5.6
2017 Sept. 20	58016.5293	17B-233	B	20	21.7 \pm 6.3
2017 Sept. 26	58022.4101	17B-233	B	20	<12.7
2017 Sept. 28	58024.6173	17B-233	B	21	<14.4
2017 Nov. 2 A	58059.3162	17B-233	B	20	<12.1
2017 Nov. 2 B	58059.4271	17B-233	B	20	15.8 \pm 7.0
2017 Nov. 3	58060.3017	17B-233	B	20	17.0 \pm 6.7
2017 Dec. 14	58101.2902	17B-233	B	38	11.7 \pm 3.5
2017 Dec. 18	58105.2878	17B-233	B	92	12.7 \pm 3.0
2017 Dec. 24	58111.2282	17B-233	B	92	15.4 \pm 2.3
2018 Jan. 1	58119.2037	17B-233	B	92	13.3 \pm 2.4
2018 Jan. 10	58128.2047	17B-233	B	92	23.2 \pm 3.7
2018 Jan. 22	58140.1580	17B-233	B	114	14.1 \pm 2.3
2019 Nov. 8	58795.4535	19B-001	D	87	<10.0
2019 Nov. 9	58796.4863	19B-001	D	85	29.8 \pm 4.1
2019 Nov. 18	58805.3810	19B-001	D	85	16.5 \pm 3.7
2019 Nov. 30	58817.4395	19B-001	D	87	<10.4
2019 Dec. 4	58821.5167	19B-001	D	87	11.1 \pm 4.1
2019 Dec. 9	58826.4409	19B-001	D	87	21.7 \pm 3.8
2019 Dec. 13	58830.2737	19B-001	D	85	12.0 \pm 3.9
2019 Dec. 16	58833.3747	19B-001	D	87	7.8 \pm 3.4
2019 Dec. 28	58845.2727	19B-001	D	85	10.5 \pm 3.1
2020 Jan. 2 A	58850.1150	19B-001	D	85	21.7 \pm 3.6
2020 Jan. 2 B	58850.2881	19B-001	D	87	21.5 \pm 3.9
2020 Jan. 6	58854.1723	19B-001	D	85	<7.4
2020 Jan. 12	58860.1315	19B-001	D	85	20.8 \pm 3.3
2020 Jan. 15	58863.2790	19B-001	D	87	9.0 \pm 3.9
2020 Jan. 16	58864.1253	19B-001	D	85	15.6 \pm 4.2
2020 Jan. 18	58866.0839	19B-001	D	85	10.3 \pm 4.3
2020 Jan. 21	58869.2363	19B-001	D	87	<8.5
2020 Jan. 22	58870.0604	19B-001	D	85	<9.1

concluded that the quiescent jet displays variability in flux density and/or in spectral shape.

In this paper, we present new radio observations of A0620–00 in quiescence taken with the VLA from 2017–2020. Our goal is to quantify the level of flux density variations from the quiescent jet to help inform future radio surveys of potential BHXB candidates, and to better understand the physical nature of the jet itself. This paper is arranged as follows: Section 2 describes the radio observations and data reduction, Section 3 contains the results on the variability of the A0620–00 radio flux density, results are discussed in Section 4, and a summary appears in Section 5.

2 RADIO OBSERVATIONS

We obtained a total of 31 observations of A0620–00 with the VLA over two separate observing programs, 17B-233 (13 observations executed from 2017 September–2018 January) and 19B-001 (18 observations from 2019 November–2020 January), which combined represent a total of 37 hours on source. All of our data were taken in X-band (8–12 GHz), using 2 \times 2 GHz basebands centred at 9.0 and 10.65 GHz (these central frequencies were chosen to avoid radio frequency interference from satellites in the Clarke Belt). During

the 17B-233 observing campaign the VLA was in B configuration (maximum baseline 11.1 km), and during the 19B-001 campaign the VLA was in D configuration (maximum baseline 1.03 km). A summary of our observations can be found in Table 1.

The time on source for individual observations in the initial observing campaign in Table 1 ranged between 20-114 minutes. We began program 17B-233 with 40 minute observing blocks that yielded ≈ 20 minutes on source per observation. This would have been a sufficient exposure time if A0620-00 displayed, on average, a radio flux density around $50 \mu\text{Jy}$ (i.e., similar to that observed by Gallo et al. 2006). However, upon preliminary inspections of the data, A0620-00 was consistently more than 2-3 times fainter than expected, so we adapted to longer observations (at the expense of fewer epochs during 17B-233). Ultimately, by the end of 17B-233 we settled on two hour observations that provided $\approx 85-90$ minutes on source, which were the observing times adopted for all epochs during the 19B-001 campaign.

During program 17B-233, 3C 48 was used as the primary calibrator to set the flux density scale, to perform delay calibrations, and to find complex bandpass solutions for 11/13 observations (3C 286 was the primary calibrator for the other two observations, with the choice of calibrator dictated by the local sidereal time at the beginning of each observation). Note, 3C 48 experienced a flare starting around January 2018, which may affect the flux density scale at the 5-10% level for the final ≈ 3 observations during the 17B-233 campaign.³ For the 19B-001 campaign, 3C 147 was used as the primary calibrator for all 18 observations. Across both campaigns, J0641-0320 was used as the secondary calibrator, where we cycled to J0641-0320 every $\approx 10-15$ minutes to solve for temporal changes in the complex gain solutions.

Data were calibrated and imaged according to standard procedures within the Common Astronomy Software Application v5.6.2-3 (CASA; McMullin et al. 2007). Initial calibrations were performed using the VLA pipeline (v5.6.2-2), followed by manual inspection of the calibrated measurement sets. In most observations, data between 11-12 GHz were heavily flagged due to interference from the Clarke Belt. If flagging was extensive, then the data were re-run through the pipeline for re-calibration. Data were then imaged using `tclean`, adopting two Taylor terms (`nterms=2`) to account for spectral dependences across the large fractional bandwidth. During the 17B-233 campaign, natural weighting was used to maximise sensitivity in the more extended B configuration (typical synthesised beam of $\theta_{\text{HPBW}} \approx 0.6$ arcsec), and for the 19B-001 campaign Briggs weighting with `robust=0.5` was used to balance sensitivity with mitigating bright side lobe artifacts in the more compact D configuration (typical synthesised beam of $\theta_{\text{HPBW}} \approx 7.2$ arcsec).

The flux density of A0620-00 was measured by fitting a point source in the image plane at the known location of A0620-00 (but allowing the position of the centre of the point source to vary). For the 17B-233 program, we achieved average rms noise levels of $\approx 6.0 \mu\text{Jy beam}^{-1}$ for observations with 20 minutes on source, $\approx 3.5 \mu\text{Jy beam}^{-1}$ for 40 minutes on source, $\approx 3.0 \mu\text{Jy beam}^{-1}$ for 90 minutes on source, and $2.3 \mu\text{Jy beam}^{-1}$ for the lone observation with 114 minutes on source. For the 19B-001 program, we achieved an average rms of $\approx 4.0 \mu\text{Jy beam}^{-1}$ for 90 minutes on source (the slightly worse σ_{rms} in 19B-001 compared to epochs during the 17B-233 program with similar exposure times is due to the more compact D configuration, and the use of Briggs versus natural weighting). Table 1 lists

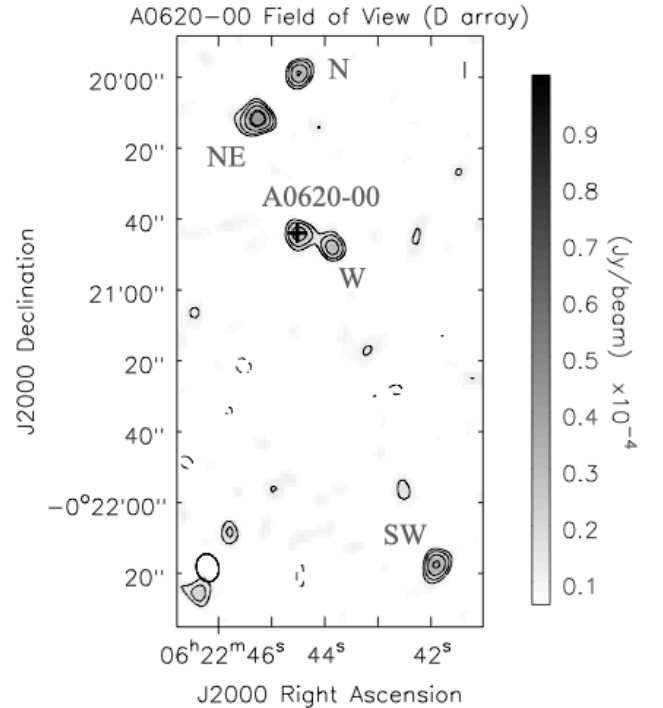


Figure 1. 9.8 GHz radio image overlaid with radio contours of the field of view surrounding A0620-00 as observed by the VLA on 2019 November 09. Contours are drawn at $\pm(\sqrt{3}^n)$ times the rms noise level of $4.0 \mu\text{Jy beam}^{-1}$, where $n = 2, 3, 4, 5, \dots$ A0620-00 is clearly detected and distinguished with cross hairs. The N and NE sources mentioned by Gallo et al. (2006) are also clearly detected and labeled. Additionally, W and SW sources are detected and labeled in this image as they are used as check sources during our analysis.

measured flux densities for each observation. Since the position of A0620-00 is well-known and radio emission has been detected previously from A0620-00 in quiescence (Gallo et al. 2006), we adopt a detection threshold of $2\sigma_{\text{rms}}$ throughout this paper. We note that this is lower than the more traditionally adopted $3\sigma_{\text{rms}}$ threshold for detection experiments. However, if the noise characteristics in the radio maps are dominated by statistical fluctuations, then the $2\sigma_{\text{rms}}$ threshold risks only a 5% chance of misidentifying a nearby noise spike as a detection. Only six of our detections fall in the $2 - 3\sigma_{\text{rms}}$ range, implying that adopting a $2\sigma_{\text{rms}}$ threshold instead of $3\sigma_{\text{rms}}$ may introduce 0.3 spurious detections (i.e., at most one false detection), which would not influence our final results. Furthermore, we find that all six of the $2 - 3\sigma_{\text{rms}}$ detections fall within 1-2 synthesized beams of the known location of A0620-00, providing further confidence that these six detections are robust.

Finally, we attempted to measure in-band spectral indices, α (where $f_\nu \propto \nu^\alpha$), for our brightest detections by splitting observations into subbands centred at 8.7 and 10.1 GHz. However, given the relatively narrow lever arm in frequency and low signal-to-noise, spectral indices have large uncertainties ($\sigma_\alpha > \pm 1$) and are not useful. We therefore do not report spectral information in this paper.

3 RESULTS

Figure 1 shows an example radio image of one of our strongest radio detections in D configuration ($29.8 \pm 4.1 \mu\text{Jy}$ on 2019 November 9), to illustrate the field of view of A0620-00, and also to note

³ <https://science.nrao.edu/facilities/vla/docs/manuals/oss/performance/fdscale>

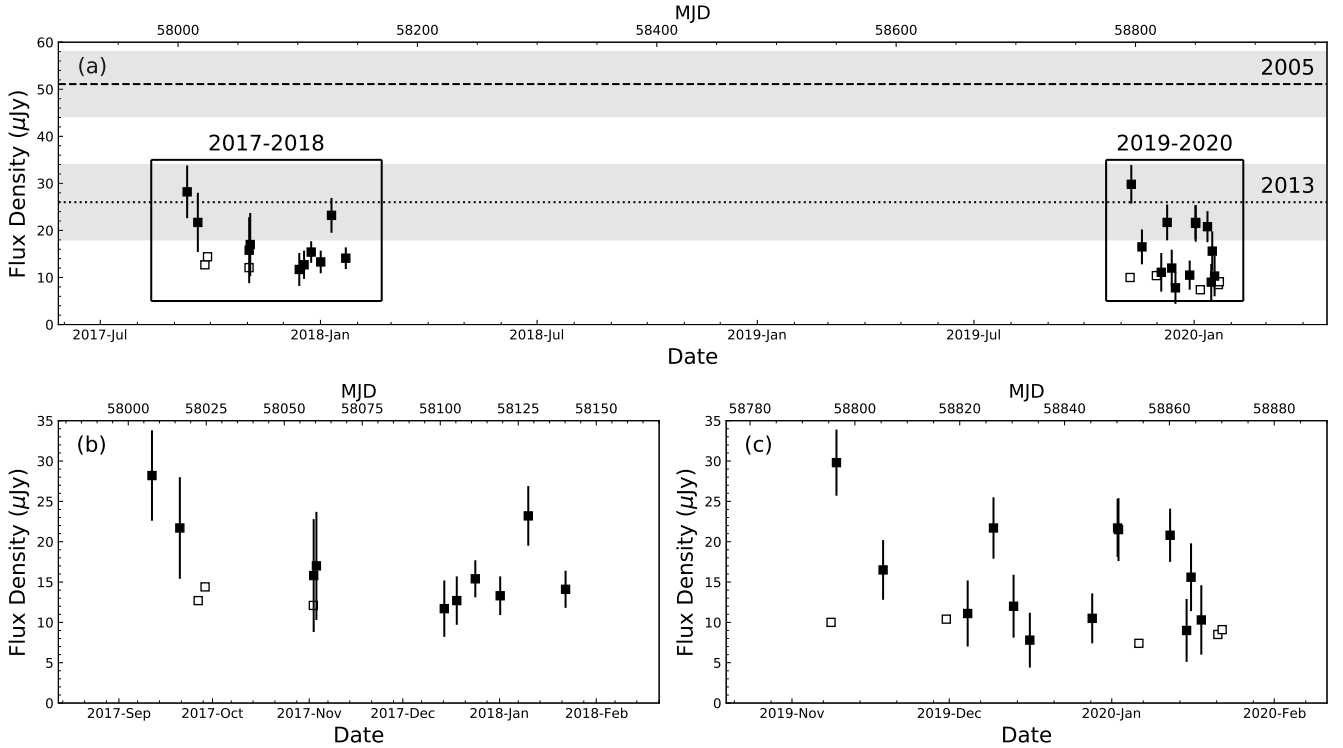


Figure 2. (a) Radio light curve of A0620–00 from 2017 September through 2020 January, at 9.8 GHz. Filled symbols represent detections, and open symbols represent $2\sigma_{\text{rms}}$ upper limits on non-detections. The horizontal dashed line marks the flux density observed in 2005 at 8.5 GHz (Gallo et al. 2006), and the horizontal dotted line marks the flux density observed in 2013 at 8.5 GHz (Dinçer et al. 2018); the grey shaded regions illustrate the $1\sigma_{\text{rms}}$ uncertainties of those measurements. (b) A zoom-in of the flux density variations during the 17B-233 observing campaign, spanning 2017 September - 2018 January. The data with larger error bars correspond to shorter times on source, which ranged from 20–114 minutes (see Table 1). (c) Data from the 19B-001 observing campaign, spanning 2019 November - 2020 January. All of these observations had approximately the same time on source (≈ 90 minutes).

the locations of four nearby field sources that we utilised as ‘check sources.’ A0620–00 did not vary in tandem with any of our check sources, indicating that observed variations of A0620–00 reflect real changes in the flux density. In Appendix A we show images for all 31 individual observations. Extended emission is never observed near A0620–00, justifying our choice to force a point source while performing flux density measurements in *imfit*. Applying our $2\sigma_{\text{rms}}$ detection threshold, eight out of the thirty-one observations are considered non-detections. We stacked the three non-detections from the 17B-233 campaign and obtained a $2\sigma_{\text{rms}}$ upper limit of $6.6 \mu\text{Jy}$. Similarly, we stacked the five non-detections from the 19B-001 campaign and obtained an upper limit of $3.7 \mu\text{Jy}$.

The 9.8 GHz light curve spanning both observing campaigns is shown in Figure 2. To quantify the distribution of flux densities observed across our entire campaign, including information from non-detections, we performed a survival analysis. We used the survival package *survfit* in R to calculate the Kaplan-Meier product-limit estimator of the logarithms of the flux densities (see, e.g., Feigelson & Nelson 1985), which calculates the survival function, $S(\log f_{9.8})$. We display this result as $1 - S(\log f_{9.8})$ in Figure 3, which represents a quantity similar to a cumulative distribution function. The median value of the survival function is $\log(f_{9.8}/\mu\text{Jy}) = 1.10$, corresponding to $\log(L_{\text{R}}/\text{erg s}^{-1}) = 26.2$. The 16-84 percentiles of the survival function provide an estimate of ± 0.22 dex for the $\pm 1\sigma$ confidence interval. We compare the observed survival function to a lognormal

distribution through a Peto & Peto test,⁴ and we find the probability for the null assumption (i.e., that the observed flux densities follow a lognormal distribution) to be $p = 0.83$. Thus, the distribution of radio flux densities is consistent with a lognormal distribution with mean $\langle \log(f_{9.8}/\mu\text{Jy}) \rangle = 1.10$ and standard deviation of ± 0.22 dex (note, the ± 0.22 dex uncertainty quantifies the level of flux variability and is not meant to represent the error on the mean). The fractional variability for the 23 detections is $F_{\text{var}} = 26 \pm 8\%$ (Vaughan et al. 2003), which represents a lower limit on the level of variability.

To further quantify variability we calculated the first-order structure function $V(\tau)$, which is one way to quantify variations in irregularly sampled data. We define the structure functions as:

$$V(\tau) = \left\langle [f(t + \tau) - f(t)]^2 \right\rangle \quad (1)$$

where $f(t)$ is the flux density at time t , and τ is the time difference between two observations. Due to the different exposure times and resulting different σ_{rms} noise levels, we were unable to calculate a useful structure function for the 2017-2018 data. In a similar vein, we did not calculate the structure function for the data spanning both observing campaigns due to the non-uniform error bars when comparing the two campaigns. Since non-detections cannot be incorporated into the structure function, the following analysis included

⁴ Specifically, we use the Peto & Peto modification of the Gehan–Wilcoxon test implemented by *cendiff* in the R package *Nondetects and Data Analysis for Environmental Data* (NADA).

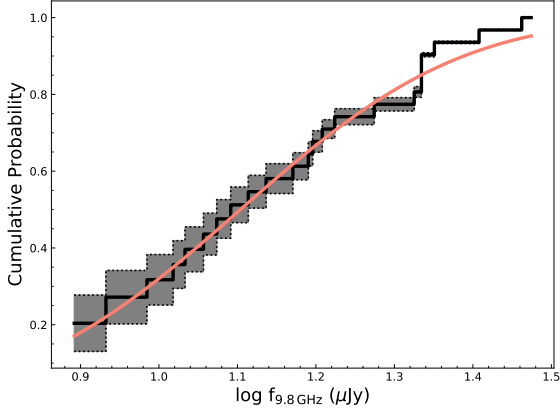


Figure 3. Cumulative distribution function (solid black histogram) of the logarithm of flux densities (9.8 GHz) for our 31 observations, plotted as $1 - S(\log \hat{f}_{9.8})$, where $S(\log \hat{f}_{9.8})$ is the survival function from the Kaplan-Meier estimator. The gray shaded region represents the $\pm 1\sigma$ uncertainty about $1 - S(\log \hat{f}_{9.8})$. The flux density is consistent with a lognormal distribution with mean $\langle \log(f_v / \mu\text{Jy}) \rangle = 1.10$ and standard deviation ± 0.22 dex, depicted by the red line.

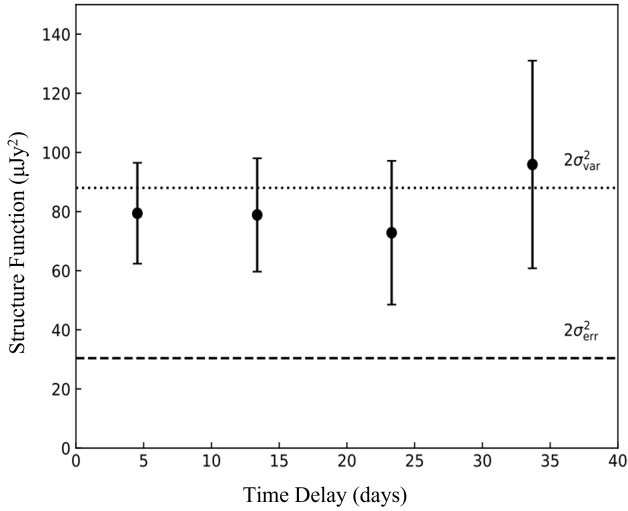


Figure 4. The first order structure function, including only the data from 2019–2020 (13 measurements, omitting non-detections). The structure function is binned to include 15 pairs of data points per time delay. The dashed horizontal line represents twice the average measurement error squared ($2\sigma_{\text{err}}^2$) and the dotted horizontal line represents twice the variance ($2\sigma_{\text{var}}^2$) of the 13 data points. Note that the dotted line is not a fit to the structure function. Flux density variations are in excess of statistical fluctuations from measurement errors. The flat slope represents either flicker noise or white noise on timescales longer than ≈ 5 days.

only the 13 detections from the 19B-001 observing campaign. We stress that this is a very small sample size for attempting a structure function analysis, but in this case it is sufficient to gain some preliminary insight into the variability characteristics of A0620–00.

Although the variations follow a lognormal distribution, we calculated the structure function in linear space to maximise the dynamic range. For every pair of detections (t_i, t_j) during the 19B-001 campaign, we defined $\tau_{ij} = t_j - t_i$ and $V_{ij}(\tau_{ij}) = [f(t_j) - f(t_i)]^2$.

The set of V_{ij} values was then binned by time delay so that each bin had 15 data points and $V(\tau)$ was calculated as the average across the data contained within each bin, where τ is the midpoint of the time delays within each bin. Figure 4 shows the resultant structure function examining variability over timescales ≈ 5 –35 days (the 19B-001 campaign lasted ≈ 75 days, and one can typically only quantify the structure function to within \approx half of the maximum time baseline). We fitted a line to the structure function and found it is consistent with a flat slope $\beta = 0.055 \pm 0.190$ that plateaus to a value consistent with $2\sigma_{\text{var}}^2 = 88.0 \mu\text{Jy}^2$, where σ_{var}^2 is the variance of the measured flux densities.

4 DISCUSSION

We present light curves of A0620–00 in quiescence from 31 VLA observations spanning 2017 September – 2020 January. In the following, we interpret all radio detections as emission from a compact jet. As discussed in Gallo et al. (2006), the radio flux density of A0620–00 is too large to be attributed to other sources of emission (e.g., the underlying accretion flow, coronal emission from the companion star, etc.). Even though A0620–00 is 2–3 fainter during our observing campaigns compared to the $\approx 50 \mu\text{Jy}$ detection in Gallo et al. (2006), their conclusions still hold. For example, consider our faintest radio detection, which is $7.8 \mu\text{Jy}$ on 2019 December 16. If this emission were to be produced by an advection dominated accretion flow (ADAF; Ichimaru 1977; Narayan & Yi 1995; Yuan & Narayan 2014), the physical size of the emission region would be on the order of 300 gravitational radii (e.g., Veledina et al. 2013). In that case, the brightness temperature would be $\approx 10^{14}$ K, which is significantly above the limit from the inverse Compton catastrophe. It is therefore not physically possible for an ADAF to produce enough radio emission.

Below, in Section 4.1 we interpret the short timescale variability, i.e. days to years, over both observing campaigns. In Section 4.2 we discuss our campaigns in context with previous observations over decade timescales.

4.1 Short-term behaviour of the radio jet

Over both campaigns, we find that flux density variations by a factor of 2–4 are common on timescales of days through years. A pair of observations from 2019 November 8–9 represents one of the most extreme variations observed during our campaign, where A0620–00 went undetected on November 8 ($< 10.0 \mu\text{Jy}$), followed by the brightest flux density observed during our campaign 25 hours later ($29.8 \pm 4.1 \mu\text{Jy}$).

From the Kaplan-Meier estimator (Figure 3), typical $\pm 1\sigma$ variations of A0620–00 at 9.8 GHz are ± 0.22 dex. The structure function of A0620–00 is flat and plateaus to $2\sigma_{\text{var}}^2$, which (a) confirms that the variations are intrinsic (i.e., they are in excess of expectations from statistical noise related to measurement error) and (b) the long-term fluctuations on 5–35 day timescales are consistent with either flicker or white noise (see Section 3.1 of Plotkin et al. 2019, and references therein, for interpretations of flat structure functions). Note, these timescales are shorter than the viscous time of the outer accretion disk, thereby implying that the radio jet variability is not mimicking changes in the mass transfer rate from the donor star to the outer disk. Qualitatively, these results are similar to those obtained by Plotkin et al. (2019) for the radio variability of V404 Cygni in quiescence (note, their structure function spanned ≈ 10 –4000 days instead of ≈ 5 –35 days for A0620–00). In the case of V404 Cygni, a small number

of flares were also observed on minute-to-hour timescales, such that [Plotkin et al. \(2019\)](#) concluded that the variability of V404 Cygni is consistent with a damped random walk, likely related to shocks propagating through a jet (e.g., [Malzac 2014](#)). Even though A0620–00 is too faint to resolve individual flares on timescales less than 1–2 hours, a similar explanation is likely. In particular, [Dinçer et al. \(2018\)](#) saw potential variability on a timescale of ≈ 2.5 hours, where the 22 GHz flux density of A0620–00 increased from $\approx 50 \pm 10$ to $\approx 80 \pm 10 \mu\text{Jy}$.⁵ If variations from the radio jet of A0620–00 indeed follow a damped random walk, then the structure function places a limit of less than 5 days on the damping timescale.

Despite the above qualitative similarities, there may be quantitative differences in that A0620–00 appears to display a lower degree of fractional variability (at 9.8 GHz) compared to V404 Cygni (at 8.4 GHz). The standard deviation of the lognormal flux density distribution of A0620–00 is ± 0.22 dex compared to ± 0.30 dex for V404 Cygni, and, more significantly, the fractional variability (in linear space) of A0620–00 is $F_{\text{var}} = 26 \pm 8\%$ compared to $F_{\text{var}} = 54 \pm 6\%$ for V404 Cygni ([Plotkin et al. 2019](#)). We note that A0620–00 has ≈ 3 times fewer data points in its quiescent radio light curve compared to the 8.4 GHz light curve of V404 Cygni. To investigate whether the smaller standard deviation and F_{var} from A0620–00 is an artifact of poorer sampling of its flux density distribution, we run Monte Carlo simulations by randomly selecting 31 data points from the 8.4 GHz light curve of V404 Cygni (89 data points) published by [Plotkin et al. \(2019\)](#).⁶ For these 31 data points, we calculate the Kaplan-Meier estimator (incorporating non-detections) and F_{var} (including only detections), and we repeat 10000 times. Results are shown in Figure 5.

The above realisations of the data with only 31 data points recover, on average, similar standard deviations of the lognormal flux density distribution (0.29 ± 0.04 dex) compared to the full V404 Cygni light curve with 89 data points (± 0.30 dex). Similar values for F_{var} are also found, on average, from our simulations ($50 \pm 9\%$) compared to the full light curve (54%). Thus, sampling a light curve with only 31 data points does not appear to significantly bias our results, within the uncertainties. Although, a small caveat is that the distribution of F_{var} values recovered by our simulations are asymmetric (see Figure 5). The mode from our simulations is 46%, which is slightly smaller than the value calculated from the full light curve (54%), albeit not at a level we consider highly significant (see further discussion below).

If A0620–00 were to have the same level of intrinsic variability as V404 Cygni, then the above simulations also allow us to quantify the probability that our campaign on A0620–00 happened to underestimate its intrinsic variability by random chance. We find that 6.0% of our simulations recover a standard deviation as small (or smaller) than the value observed from A0620–00 (± 0.22 dex), and 0.03% of our simulations recover an F_{var} value as small as observed from A0620–00 (26%). Thus, if A0620–00 has similar levels of intrinsic radio variability as V404 Cygni, it is plausible that the poorer sampling of the A0620–00 light curve could yield the smaller observed

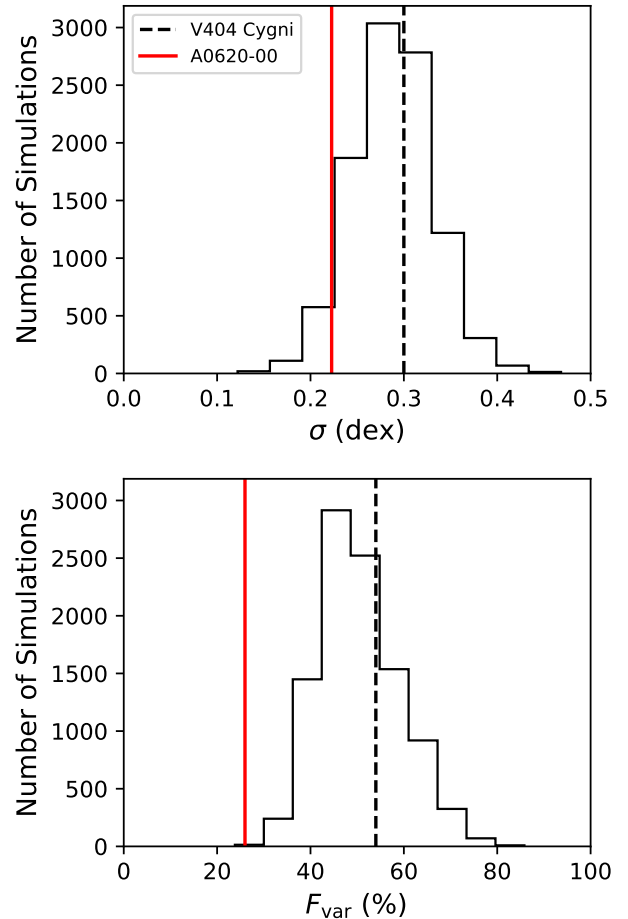


Figure 5. Black histograms show results from 10000 Monte Carlo simulations randomly drawing 31 data points from the 8.4 GHz radio light curve of V404 Cygni from [Plotkin et al. \(2019\)](#). *Top panel:* the standard deviation of each realisation of the V404 Cygni light curve, parameterised by the 16–84 percentile range of the survival function from the Kaplan-Meier distribution. The vertical black dashed line shows the value calculated by [Plotkin et al. \(2019\)](#) from the full light curve, and the vertical solid red line shows the value calculated for A0620–00 in this paper. *Bottom panel:* the distributions of F_{var} values calculated from the 10000 Monte Carlo simulations. The black dashed and solid red vertical lines have the same meanings as in the top panel. These simulations suggest that the lower level of variability observed from A0620–00 compared to V404 Cygni is unlikely an artifact of the poorer sampling of the A0620–00 light curve, especially for F_{var} .

standard deviation; however, the poorer sampling is very unlikely the primary driver for the lower observed value of F_{var} . Note, both the A0620–00 and V404 Cygni light curves have a similar fraction of non-detections ($8/31=26\%$ for A0620–00 versus $25/89=28\%$ for V404 Cygni), so the above results are unlikely suffering from systematics related to the survival analysis and/or only including detections in the F_{var} calculation. Thus, A0620–00 appears to indeed be (slightly) less variable than V404 Cygni. This result could imply that lower luminosity jets are less variable. Confirmation will require performing similar campaigns on other quiescent BHXBs (which will require more sensitive radio facilities, and/or discovering new BHXBs at close enough distances to detect their quiescent radio jets; see, e.g., [Rodriguez et al. 2020](#)). Confirmation of this result would have favourable implications for variability inducing

⁵ Our campaign was generally insensitive to intraday variability, except for a pair of observations taken on 2017 November 2 separated by ≈ 2.6 hours, and a pair on 2020 January 2 separated by ≈ 4 hours. Only the 2017 November 2 observations may hint at short-term variability, where we obtained a non-detection ($< 12.1 \mu\text{Jy}$) followed by a detection ($15.8 \pm 7.0 \mu\text{Jy}$), but we do not consider this to be statistically significant.

⁶ Note, there is insufficient coverage of V404 Cygni for us to also attempt to replicate the observing cadence of A0620–00 over a 3–4 month period. Thus we do not attempt to simulate the effect that fewer data points will have on the structure function.

less severe systematics (at low luminosities) when searching for new BHXB candidates via their radio jets.

4.2 Long-term behaviour of the radio jet

We conclude the discussion by using our variability constraints to attempt to better understand the long-term behaviour of A0620-00's radio jet. Previous detections of the radio outflow (at GHz frequencies) include the $51.1 \pm 6.9 \mu\text{Jy bm}^{-1}$ detection in 2005 at 8.5 GHz by Gallo et al. (2006), and the $26 \pm 8 \mu\text{Jy}$ detection in 2013 at 8.5 GHz, based on the broadband spectrum observed by Dinçer et al. (2018). The average 9.8 GHz flux density from our 17B-233 program (2017 September – 2018 January) is $17.3 \pm 1.5 \mu\text{Jy bm}^{-1}$, and the average flux density from our 19B-001 program (2019 November – 2020 January) is $16.0 \pm 1.1 \mu\text{Jy bm}^{-1}$ (note, the uncertainties reported for these average flux densities are the error on the mean).

It is striking how much brighter the radio jet was during its discovery in 2005, and that over ≈ 30 subsequent observations (covering nearly 15 years) the jet has never been observed to be so bright again. One interpretation is a gradual, long-term dimming of the radio jet (the differences in observing frequencies above would result in additional $\lesssim 10\%$ systematic uncertainties, adopting the inverted spectral index $\alpha = 0.74 \pm 0.19$ measured by Dinçer et al. 2018). Alternatively, stochastic variability cannot be excluded, which would imply that the discovery in 2005 fortuitously caught A0620-00 during a relatively bright flare. The 2005 observation, $\log(f_{9.8}/\mu\text{Jy}) = 1.71$, represents a 3σ deviation from the mean of our Kaplan-Meier distribution, thus yielding a 0.15% chance of finding the source at least this bright by random chance (assuming one can safely extrapolate our observed flux density distribution to higher flux densities). This is a small but non-negligible probability. For the 2013 observations, interpolating the flux density reported by Dinçer et al. (2018) from 8.5 to 9.8 GHz, that observation would have $\log(f_{9.8}/\mu\text{Jy}) = 1.46$. Our Kaplan-Meier distribution suggests a 2.8% chance of observing A0620-00 at $\log(f_{9.8}/\mu\text{Jy}) > 1.46$.

Our constraints on the level of variability at 9.8 GHz are also helpful for interpreting broadband spectra of quiescent jets. For example, Gallo et al. (2019) detected an apparently steep sub-millimetre spectrum from A0620-00 using the ALMA, based on detections at 98 GHz ($44 \pm 7 \mu\text{Jy}$) and at 233 GHz ($20 \pm 8 \mu\text{Jy}$). As pointed out by Gallo et al. (2019), the observations at these two frequencies were performed 40 days apart, such that a factor of ≈ 2 variability would be sufficient to influence the observed sub-millimetre spectrum. Given that such variability is common from A0620-00 at GHz frequencies, our campaign supports the conclusion of Gallo et al. (2019) that jet variability is one plausible explanation, especially when considering that compact synchrotron jets are expected to be more variable at higher frequencies (Tetarenko et al. 2019, 2021).

5 SUMMARY

We presented a monitoring campaign on the radio jet launched by the quiescent BHXB A0620-00, spanning 2017 September – 2018 January and 2019 November – 2020 January, with a total of 31 observations representing 37 hours on source. These observations comprise the most intense radio monitoring campaign yet on A0620-00, which we use to provide statistical constraints on the radio variability of one of the least luminous BHXB jets. We find flux densities that follow a lognormal distribution, with a mean $\langle \log(f_\nu/\mu\text{Jy}) \rangle = 1.10$ and a standard deviation of ± 0.22 dex at 9.8 GHz (the average flux density corresponds to a radio luminosity at 9.8 GHz of $L_R \approx 2 \times 10^{26}$ erg

s^{-1}). Factor of 2–4 flux density variations are common on timescales ranging from days to years, and we quantify the fractional variability to be at least $F_{\text{var}} = 26 \pm 8\%$. Over the data collected between 2019–2020, A0620-00 displays a flat structure function, indicating that the observed flux density variations are consistent with either flicker noise or white noise on timescales 5–35 days. Intriguingly, none of our observations found A0620-00 to be as bright as during its discovery observation in 2005, implying either a long-term dimming of the radio jet, or the 2005 observations happened to catch A0620-00 during a relatively bright flare. The variability characteristics of A0620-00 are similar to V404 Cygni, the only other BHXB for which radio variability has been similarly quantified in quiescence, except that A0620-00 may be slightly less variable (e.g., V404 Cygni follows a lognormal flux density distribution at 8.4 GHz with a standard deviation of $\approx \pm 0.3$ dex and $F_{\text{var}} = 54 \pm 6\%$). This lower level of variability from A0620-00 may indicate that lower luminosity quiescent jets could be less variable at GHz frequencies.

Understanding the level of jet variability is important for being able to interpret broadband spectra built with non-simultaneous multiwavelength data (e.g., Gallo et al. 2007, 2019), and it also has implications for using radio surveys, in conjunction with non-simultaneous multiwavelength information, to uncover new populations of quiescent BHXBs (e.g., Maccarone 2005). Further monitoring of A0620-00 will be useful to better sample its flux density distribution and improve our statistical calculations, and it would be worthwhile to repeat such a study at other frequencies. To improve our understanding of quiescent BHXB jet variability, however, will ultimately require discovering more nearby systems, or else await new generations of radio telescopes such as a next generation VLA (ngVLA) or the Square Kilometre Array (SKA-MID). A facility like an ngVLA in particular, which would have an order of magnitude improvement in sensitivity compared to the VLA, would allow us to significantly expand the number of feasible targets, while also opening up searches for flaring activity (on minute-to-hour time scales) from jets as faint as A0620-00.

ACKNOWLEDGEMENTS

We thank the anonymous referee for constructive comments that improved the manuscript. The National Radio Astronomy Observatory is a facility of the National Science Foundation operated under cooperative agreement by Associated Universities, Inc. This research made use of Astropy,⁷ a community-developed core Python package for Astronomy (Astropy Collaboration et al. 2013, 2018). J.C.A.M.-J. was supported by an Australian Research Council Future Fellowship (FT140101082). J.S. acknowledges support from the Packard Foundation.

DATA AVAILABILITY

The data that supported the findings of this study are available at the National Radio Astronomy Observatory archive at data.nrao.edu under the project codes: 17B-233 and 19B-001.

REFERENCES

Abbott B. P., et al., 2016, *Phys. Rev. Lett.*, **116**, 061102

⁷ <http://www.astropy.org>

- Astropy Collaboration et al., 2013, *A&A*, **558**, A33
- Astropy Collaboration et al., 2018, *AJ*, **156**, 123
- Bernardini F., Cackett E. M., 2014, *MNRAS*, **439**, 2771
- Blandford R. D., Königl A., 1979, *ApJ*, **232**, 34
- Cantrell A. G., et al., 2010, *ApJ*, **710**, 1127
- Carotenuto F., Corbel S., Tzioumis A., 2022, arXiv e-prints, p. [arXiv:2208.00100](https://arxiv.org/abs/2208.00100)
- Casares J., 2018, *MNRAS*, **473**, 5195
- Chomiuk L., Strader J., Maccarone T. J., Miller-Jones J. C. A., Heinke C., Noyola E., Seth A. C., Ransom S., 2013, *ApJ*, **777**, 69
- Corbel S., Fender R. P., 2002, *ApJ*, **573**, L35
- Dinçer T., Bailyn C. D., Miller-Jones J. C. A., Buxton M., MacDonald R. K. D., 2018, *ApJ*, **852**, 4
- Dzib S. A., Massi M., Jaron F., 2015, *A&A*, **580**, L6
- Eachus L. J., Wright E. L., Liller W., 1976, *ApJ*, **203**, L17
- Elvis M., Page C. G., Pounds K. A., Ricketts M. J., Turner M. J. L., 1975, *Nature*, **257**, 656
- Feigelson E. D., Nelson P. I., 1985, *ApJ*, **293**, 192
- Fender R. P., 2001, *MNRAS*, **322**, 31
- Froning C. S., et al., 2011, *ApJ*, **743**, 26
- Gallo E., Fender R. P., Hynes R. I., 2005, *MNRAS*, **356**, 1017
- Gallo E., Fender R. P., Miller-Jones J. C. A., Merloni A., Jonker P. G., Heinz S., Maccarone T. J., van der Klis M., 2006, *MNRAS*, **370**, 1351
- Gallo E., Migliari S., Markoff S., Tomsick J. A., Bailyn C. D., Berta S., Fender R., Miller-Jones J. C. A., 2007, *ApJ*, **670**, 600
- Gallo E., et al., 2014, *MNRAS*, **445**, 290
- Gallo E., et al., 2019, *MNRAS*, **488**, 191
- Giesers B., et al., 2019, *A&A*, **632**, A3
- González Hernández J. I., Rebolo R., Casares J., 2014, *MNRAS*, **438**, L21
- Hjellming R. M., Rupen M. P., Mioduszewski A. J., Narayan R., 2000, *The Astronomer's Telegram*, **54**, 1
- Hynes R. I., Bradley C. K., Rupen M., Gallo E., Fender R. P., Casares J., Zurita C., 2009, *MNRAS*, **399**, 2239
- Ichimaru S., 1977, *ApJ*, **214**, 840
- Jonker P. G., et al., 2014, *ApJS*, **210**, 18
- Jonker P. G., Kaur K., Stone N., Torres M. A. P., 2021, *ApJ*, **921**, 131
- Maccarone T. J., 2005, *MNRAS*, **360**, L30
- Malzac J., 2014, *MNRAS*, **443**, 299
- McClintock J. E., Remillard R. A., 1986, *ApJ*, **308**, 110
- McMullin J. P., Waters B., Schiebel D., Young W., Golap K., 2007, in Shaw R. A., Hill F., Bell D. J., eds, *Astronomical Society of the Pacific Conference Series Vol. 376, Astronomical Data Analysis Software and Systems XVI*, p. 127
- Miller-Jones J. C. A., Gallo E., Rupen M. P., Mioduszewski A. J., Brisken W., Fender R. P., Jonker P. G., Maccarone T. J., 2008, *MNRAS*, **388**, 1751
- Miller-Jones J. C. A., Jonker P. G., Dhawan V., Brisken W., Rupen M. P., Nelemans G., Gallo E., 2009, *ApJ*, **706**, L230
- Miller-Jones J. C. A., Jonker P. G., Maccarone T. J., Nelemans G., Calvelo D. E., 2011, *ApJ*, **739**, L18
- Miller-Jones J. C. A., et al., 2015, *MNRAS*, **453**, 3918
- Narayan R., McClintock J. E., 2005, *ApJ*, **623**, 1017
- Narayan R., Yi I., 1995, *ApJ*, **452**, 710
- Plotkin R. M., Gallo E., Jonker P. G., 2013, *ApJ*, **773**, 59
- Plotkin R. M., et al., 2016, *MNRAS*, **456**, 2707
- Plotkin R. M., Miller-Jones J. C. A., Chomiuk L., Strader J., Bruzewski S., Bundas A., Smith K. R., Ruan J. J., 2019, *ApJ*, **874**, 13
- Plotkin R. M., Bahramian A., Miller-Jones J. C. A., Reynolds M. T., Atri P., Maccarone T. J., Shaw A. W., Gandhi P., 2021, *MNRAS*, **503**, 3784
- Rana V., et al., 2016, *ApJ*, **821**, 103
- Ribó M., et al., 2017, *ApJ*, **835**, L33
- Rodríguez J., et al., 2020, *ApJ*, **889**, 58
- Shishkovsky L., et al., 2018, *ApJ*, **855**, 55
- Shishkovsky L., et al., 2020, *ApJ*, **903**, 73
- Strader J., Chomiuk L., Maccarone T. J., Miller-Jones J. C. A., Seth A. C., 2012, *Nature*, **490**, 71
- Tetarenko B. E., et al., 2016, *ApJ*, **825**, 10
- Tetarenko A. J., et al., 2019, *MNRAS*, **482**, 2950
- Tetarenko A. J., et al., 2021, *MNRAS*, **504**, 3862
- Thompson T. A., et al., 2019, *Science*, **366**, 637
- Tremou E., et al., 2020, *MNRAS*, **493**, L132
- Tudor V., et al., 2022, *MNRAS*,
- Urquhart R., et al., 2020, *ApJ*, **904**, 147
- Vaughan S., Edelson R., Warwick R. S., Uttley P., 2003, *MNRAS*, **345**, 1271
- Veledina A., Poutanen J., Vurm I., 2013, *MNRAS*, **430**, 3196
- Yuan F., Narayan R., 2014, *ARA&A*, **52**, 529
- Zhao Y., et al., 2020, *MNRAS*, **493**, 6033

APPENDIX A: IMAGES OF INDIVIDUAL OBSERVATIONS

Below we show images of each observation in our 17B-233 (Figure A1) and 19B-001 campaigns (Figure A2).

This paper has been typeset from a $\text{\TeX}/\text{\LaTeX}$ file prepared by the author.

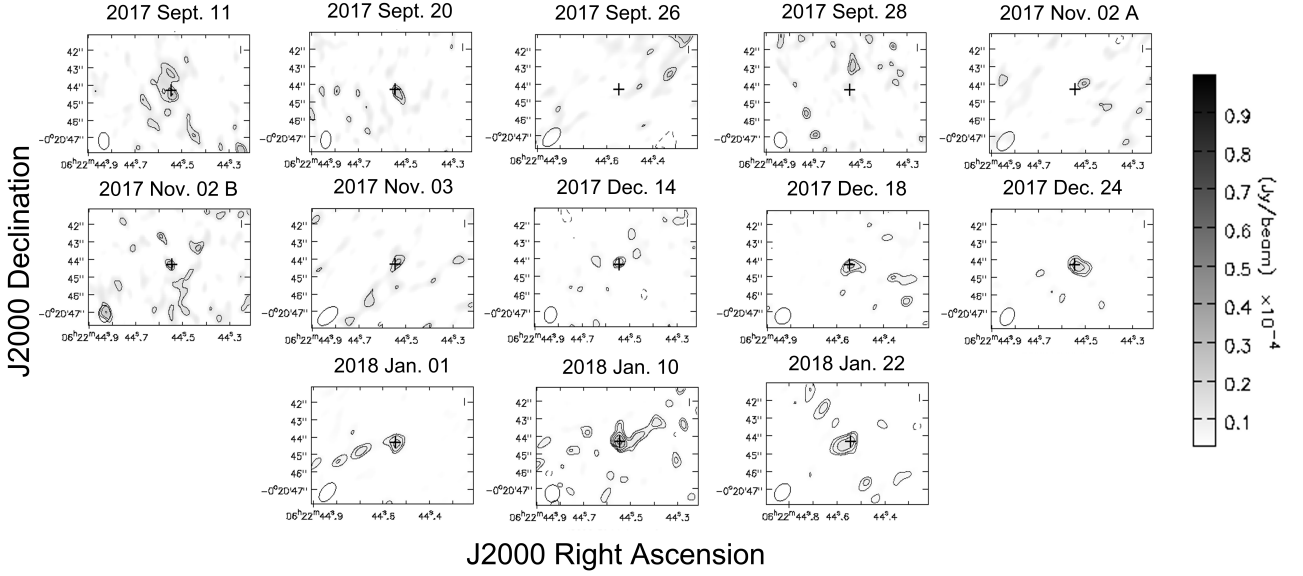


Figure A1. Contour images summarising the detections and non-detections of A0620–00 from the 17B-233 observing campaign. The coordinates of A0620–00 are marked in each panel with cross hairs. Since the images from 2017–2018 had different exposure times, the contours for each panel correspond to the average σ_{rms} with respect to the exposure time. For 20 minutes time on source (t.o.s.) (2017 September 11 – 2017 November 3), contours are at $\pm(\sqrt{2}^n)$ times the σ_{rms} of $6.0 \mu\text{Jy beam}^{-1}$, with $n = 2, 3, 4, 5, \dots$. For 40 minutes t.o.s. (2017 December 14), contours are similarly scaled to $\sigma_{\text{rms}} = 3.5 \mu\text{Jy beam}^{-1}$. For 90 minutes t.o.s. (2017 December 18 – 2018 January 10), contours are scaled to $\sigma_{\text{rms}} = 3.0 \mu\text{Jy beam}^{-1}$. Finally, for 115 minutes t.o.s. (2018 January 22), contours are scaled to $\sigma_{\text{rms}} = 2.3 \mu\text{Jy beam}^{-1}$. The non-detections for this campaign are 2017 September 26, 2017 September 28, and 2017 November 02 A.

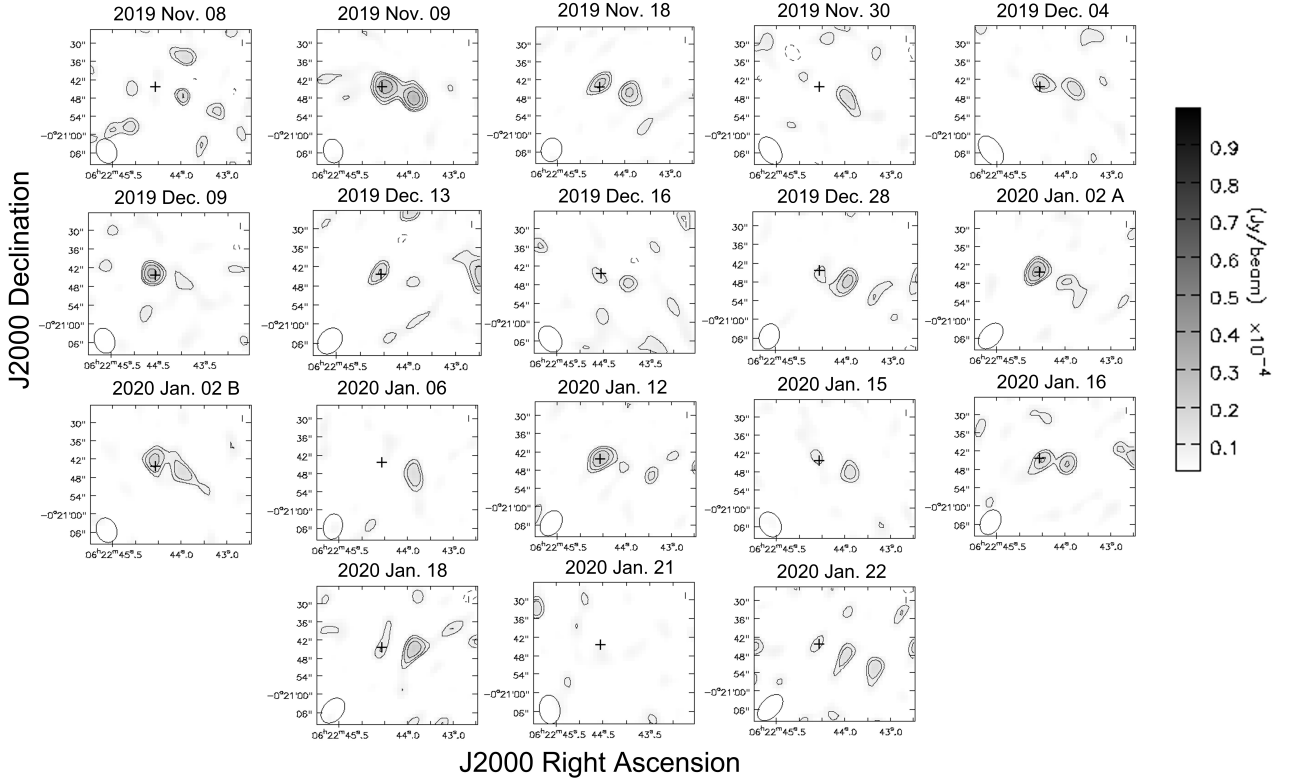


Figure A2. Contour images summarising the detections and non-detections of A0620–00 from the 19B-001 observing campaign. The coordinates of A0620–00 are marked in each panel with cross hairs. Since the images from 2019–2020 all had the same time on source of 90 minutes, the contours are at $\pm(\sqrt{2}^n)$ times the σ_{rms} of $4.0 \mu\text{Jy beam}^{-1}$, with $n = 2, 3, 4, 5, \dots$. The non-detections for this campaign are 2019 November 08, 2019 November 30, 2020 January 06, 2020 January 21, and 2020 January 22. Note that in the panel above, 2020 January 22 appears to be a detection, however σ_{rms} for this image was higher than average, making the appearance of a detection in the image when the flux density was actually below the 2σ limit on this particular date.